

# Deployment of Objects with a Soft Everting Robot

Ethan DeVries\*, Jack Ferlazzo, Mustafa Ugur, Laura H. Blumenschein

**Abstract**—Soft everting robots present significant advantages over traditional rigid robots, including enhanced dexterity, improved environmental interaction, and safe navigation in unpredictable environments. While soft everting robots have been widely demonstrated for exploration type tasks, their potential to move and deploy payloads in such tasks has been less investigated, with previous work focusing on sensors and tools for the robot. Leveraging the navigation capabilities, and deployed body, of the soft everting robot to deliver payloads in hazardous areas, e.g. carrying a water bottle to a person stuck under debris, would represent a significant capability in many applications. In this work, we present an analysis of how soft everting robots can be used to deploy larger, heavier payloads through the inside of the robot. We analyze both what objects can be deployed and what terrain features they can be carried through. Building on existing models, we present methods to quantify the effects of payloads on robot growth and self-support, and develop a model to predict payload slip. We then experimentally quantify payload transport using soft everting robot with a variety of payload shapes, sizes, and weights and though a series of tasks: steering, vertical transport, movement through holes, and movement across gaps. Overall, the results show that we can transport payloads in a variety of shapes and up to 1.5 kg in weight and that we can move through circular apertures with as little as 0.01 cm clearance around payloads, carry out discrete turns up to  $135^\circ$ , and move across unsupported gaps of 1.15 m in length.

**Index Terms**—Soft Robot Materials and Design, Soft Robot Applications

## I. INTRODUCTION

The field of soft robotics has shown that compliance and novel locomotion modes can be used to navigate complex environments [1]–[3]. One versatile class of soft robots is the soft everting robot (i.e. Vine Robots [4], [5]), which extends its body by everting a thin, flexible tube from its tip while remaining tethered to a base station. Only the tip moves during growth, reducing friction and environmental disturbance [6]. Soft everting robots have been shown to traverse highly constrained and cluttered spaces, making them promising for use in search-and-rescue operations [7], medical procedures [8], and exploration of underwater or underground environments [9], [10]. While many sensing and actuation strategies have been developed for soft everting robots [4], [11], significant challenges remain, especially in leveraging the unique capabilities of the robot to carry payloads. Recent studies have addressed some interaction limitations, including stronger eversion drives for higher force output [12] and tip attachments for sensors and grippers [13]–[16]. However, these works still use the soft everting robot tip to carry objects,

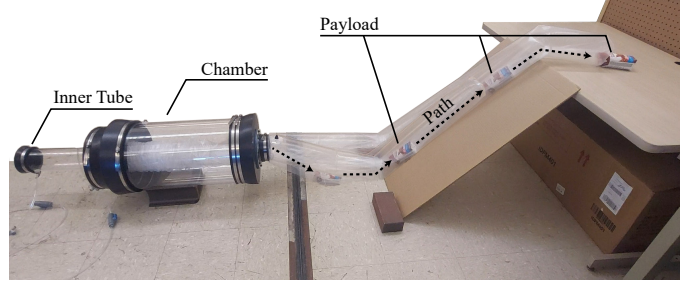


Figure 1. Soft everting robot carrying an object up a 45-degree slope.

limiting the carrying capacity and increasing the frictional interaction of the robot with the environment.

A similar class of robots, everting grippers [17]–[21], suggests a different way to deploy objects with these robots. Everting grippers grasp by everting and inverting a membrane around a target, generating holding forces through pressure, surface friction, and object geometry. If we imagine a soft everting robot as an extended everting gripper, payload deployment can be achieved by everting the internal membrane.

Early demonstrations of soft everting robots used the internal channel for small lightweight payloads, like small cameras and wires [6], [22]. However, this required access to the internal working channel to continually pull back on wires as the robot grew [5]. As a result, this approach could not be used in designs which stored the material on a spool, thereby sealing off the one end of the central working channel. An alternative base design, an origami-inspired mechanism, introduced a way to compactly store material while maintaining a working channel for a camera and wire [23], and subsequent work redesigned the everting robot to open the channel and pass tools without friction [24]. These efforts have focused on tools extended through the channel, not analyzing the robot's ability to grasp, transport, or deploy payloads, as recently shown [25].

This paper extends these previous works to present a characterization of payload deployment using the internal material stream, or tail, of a soft everting robot to grasp, carry, and deploy objects while isolating them from the environment. The tubular body encapsulates a payload and it is moved forward toward the robot tip by eversion. We will show the range of payload geometries and weights which can be deployed, and how and when payload deployment affects soft everting robot movement. The remainder of this paper is organized as follows. Section II reviews the existing origami-inspired soft everting robot designs [23] and discusses our adaptations for internal object deployment. Section III then derives the effects of payloads on soft everting robot and gripper analytical models in order to predict successful deployment. We experimentally validate these models and demonstrate payload transportation in Section IV and discuss results in Section V.

This work is supported in part by National Science Foundation grant 2308653

All authors are with the School of Mechanical Engineering, Purdue University, 47907, IN, USA. \*Corresponding author. { edevrie, jferlazz, mugur, lhblumen}@purdue.edu

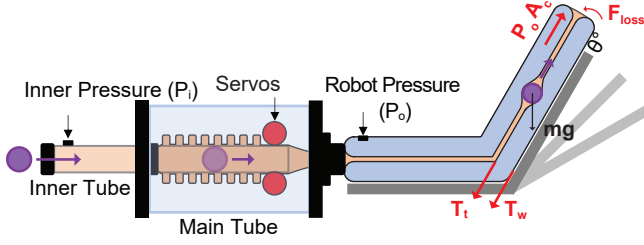


Figure 2. Payload-capable soft everting robot. The inner tube is pressurized to  $P_i$  (orange) and the surrounding chamber to  $P_o$  (blue). Forces acting during growth while carrying an internal payload are shown.

## II. DESIGN OVERVIEW

In this section, we review the design concept for a soft everting robot with an accessible internal working chamber, first demonstrated by Ryu et al. [23], and discuss the materials and modifications made to deploy a variety of payloads. The origami-inspired mechanism replaces the previously used spool with a stack of origami folds wrapped around a rigid inner tube (Fig. 2). Since the far end of material is attached to the inner tube, the central chamber remains open, allowing objects equal to or smaller than the inner tube to pass from the base to the tip throughout deployment. Servos are used to supply and retract the membrane from the tube. The inner material applies a pressure envelope around any objects inside, pulling them along as the robot everts. This pressure is also applied on the inner tube, increasing friction. The inner tube can be pressurized and this inner pressure, plus the servos, helps with breaking the friction on the stored material.

To deploy individual payloads with the system, we primarily need to increase the size of the inner tube and make the outside end unsealable, so payloads can be added throughout growth. We aim to deliver payloads around the size of a water bottle, i.e. objects around 6 cm in diameter, so we use an inner tube diameter,  $D_t$ , of 10.2 cm. We must also increase the diameter of the robot,  $D_{\text{robot}}$ , to accommodate, increasing to 13 cm. To compare to the earlier work, we can take the ratio of  $D_t$  and  $D_{\text{robot}}$ : we have  $D_{\text{robot}}/D_t \approx 1.27$  compared to original work where  $D_{\text{robot}} = 5$  cm,  $D_t = 1.3$  cm so  $D_{\text{robot}}/D_t = 3.8$ . The remainder of the materials to construct the soft everting robot are as follows. The inner tube and chamber tube are made of polymethyl methacrylate (PMMA) (i.e. acrylic) tubes and all end caps are modified QwikCaps. The soft everting robot is made from a 0.0508 mm thick Low-Density PolyEthylene (LDPE) tube. A low-friction ultra-high-molecular-weight polyethylene (UHMW) material lined the inner tube to lower friction. Two high-torque continuous-rotation servos (DYNAMIXEL XM540-W270-T, stall torque 10.6 N m at 12 V, no-load speed 30 rpm) were installed to pinch the membrane between silicone rollers and the tube and thereby overcome the remaining friction. The pressures in both inner and main tubes were controlled by QB3 pressure controllers and the robot pressure,  $P_o$  was measured by Honeywell Sensing 5 psi (SSCDANN005PGAA5) pressure sensor. Note, unless specified, the inner pressure,  $P_i$ , is the commanded pressure.

## III. MODELING

This section develops quasi-static models to describe how a soft everting robot can carry internal payloads. These models answer: 1) can the robot still grow, 2) can the robot hold the object without it slipping, and 3) can the robot move without buckling? The models below build on existing soft everting robot models and give the tools to evaluate the deployment.

### A. Object Transportation

In general, growth of a soft everting robot initiates when the pressure force at the tip overcomes the resisting tensions and minimum growth force, as shown by Coad *et al.* [26]:

$$P_o A_c = 2T_t + F_{\text{loss}}. \quad (1)$$

where  $A_c = \frac{\pi}{4} D_{\text{robot}}^2$  is the tip cross sectional area,  $T_t$  is the tail tension,  $F_{\text{loss}}$  is the frictional loss at the tip during eversion, and  $P_o$  is the measured internal pressure. When the control system specifies a set pressure, pressure over the minimum value will be lost to friction proportional to air flow rate and to growth velocity [6]. Since the robot must also convey a payload, this will add resisting tension. While on a horizontal surface the payload weight has a negligible effect on growth, when a payload of mass  $m_{\text{payload}}$  is moved in the vertical direction, e.g. up an incline of angle  $\theta$ , the driving pressure must additionally lift that mass, giving

$$P_o A_c = 2T_t + F_{\text{loss}} + m_{\text{payload}} g \sin \theta. \quad (2)$$

where  $g$  is the acceleration due to gravity, and  $\theta$  is the slope angle. Without servo assistance, the  $T_t$  is produced by friction between the folded membrane and the inner tube:

$$T_t = (P_o - P_i) \mu_t (A_t + \frac{1}{2} A_c \cos \phi), \quad (3)$$

where  $A_t = \pi D_t L_t$  is the tube surface area,  $L_t$  is the tube length,  $\phi$  is the wrap angle as defined below (Equation (9)), and  $\mu_t \approx 0.41$  is the robot to tube friction coefficient. Here  $P_i$  denotes the commanded pressure; since the robot tip is open to atmosphere, in many cases the true pressure is much lower and the internal pressure will not overcome friction.

Instead, we include the tail-drive servos, which move at a set speed. Two limiting cases arise. If the servos are faster than the robot ( $v_{\text{servo}} > 2v_{\text{robot}}$ ), the tail is slack ( $T_t \approx 0$ ). If they are slower, neglecting velocity dependence, the robot pressure will equal set pressure, and the tension becomes

$$T_t \approx \frac{1}{2} (P_o A_c - F_{\text{loss}} - m_{\text{payload}} g \sin \theta). \quad (4)$$

The maximum robot speed,  $v_{\text{robot}}$ , will derive from the maximum chamber flow rate  $\dot{Q}_{\text{chamber}}$ :

$$v_{\text{robot}} = \frac{\dot{Q}_{\text{chamber}}}{A_c}. \quad (5)$$

With material slack ( $T_t = 0$ ), the robot pressure reduces to

$$P_o > \frac{F_{\text{loss}} + m_{\text{payload}} g \sin \theta}{A_c}. \quad (6)$$

The model for robot pressure needed to grow is in Table I.

Table I  
SUMMARY OF THE MODELING EQUATIONS FOR PAYLOAD DEPLOYMENT

Object Transportation	Object Grasping	Unsupported Gaps
$P_o = \begin{cases} \frac{F_{\text{loss}} + m_{\text{payload}} g \sin \theta}{A_c}, & \text{if } v_{\text{servo}} > 2v_{\text{robot}}, \\ \text{Set Pressure}, & \text{if } 2v_{\text{robot}} > v_{\text{servo}}. \end{cases}$	$K = 1 \times 10^{-5} \mu (A_w + \frac{1}{2} A_c \cos \phi)$ $\phi \approx \arccos \left( \frac{2D_{\text{payload}}^2}{D_{\text{robot}}^2} \left( 1 - \frac{P_i}{P_o} \right) \right)$	$L_{\text{robot}} = \sqrt{\frac{\frac{P_o \pi D_{\text{robot}}^3}{8} - m_{\text{payload}} g d_{\text{payload}}}{\pi D_{\text{robot}} t \rho g}}$

### B. Object Grasping

To determine when objects can be held without slipping, we treat the robot as an everting gripper [17]–[21]. Building off the grasping model by Sui *et al.* [18], the pull-out force, i.e. the maximum axial load before an object slips, comes from a combination of Coulomb friction and tension due to the wrap angle from the membrane. In this study, we reframe this pull-out force as the payload weight that can be transported without slip.

The grip strength should be directly proportional to pressure, so we define the effective grip contact area  $K$  as the ratio of force increase as a result of pressure increase,  $K = \frac{\Delta F}{\Delta P}$ , [NkPa<sup>-1</sup>].

The effective contact area will be [18]:

$$K = 1 \times 10^{-5} \mu (A_w + \frac{1}{2} A_c \cos \phi), \quad (7)$$

where  $A_w$  [m<sup>2</sup>] is wetted contact area,  $\mu$  is the contact friction coefficient, and  $\phi$  is the average wrap angle of the material around the object. The wrap angle can be found from considering the force balance radially:

$$T_t \cos \phi = (P_o - P_i) A_r \cos \phi \quad (8)$$

with  $A_r$  being the surface area of the plastic as it goes from touching the object to being fully collapsed. This equation balances the inward pull due to the pressure difference with the outward pull due to the material tension. We assume that the material forms a cone as it comes off the object, so  $A_r = \pi D_{\text{payload}}^2 / 4 \cos \phi$ , where  $D_{\text{payload}}$  is the payload diameter. This tail tension is the same as in Equation (4), but without the object weight. For tests where the robot is not growing,  $F_{\text{loss}}$  will also be zero so  $T_t = \frac{1}{2} P_o A_c$ . Plugging this value in to Equation (8) and solving for  $\phi$  gives

$$\phi \approx \arccos \left( \frac{2D_{\text{payload}}^2}{D_{\text{robot}}^2} \left( 1 - \frac{P_i}{P_o} \right) \right). \quad (9)$$

The last unknown for Equation (7) is the wetted contact area  $A_w$ , which includes only where the material touches and therefore depends on the object geometry (see Figure 6).

### C. Buckling over Unsupported Gaps

Soft everting robot can self-support to span gaps and climb walls, with only slight bending under gravity. However, the structure will buckle under sufficient weight, either due to the span being too long or the payload too heavy. Previous analyses of pressurized soft beams [27]–[29] defined a critical bending moment,  $M_{\text{collapse}}$ , of:

$$M_{\text{collapse}} = \frac{P_o \pi D_{\text{robot}}^3}{8}. \quad (10)$$

During horizontal growth, the body can be idealized as a thin uniform cylinder of mass  $m_{\text{robot}}$  and length  $L_{\text{robot}}$ . Note, since the material in a soft everting robot is doubled back on itself, the total mass will be based off material of length  $2L_{\text{robot}}$ . This gives the weight-induced moment  $M_{\text{weight}}$  [29]

$$M_{\text{weight}} = m_{\text{robot}} g \frac{L_{\text{robot}}}{2}, \quad m_{\text{robot}} = 4\pi D_{\text{robot}} t L_{\text{robot}} \rho. \quad (11)$$

where  $\rho$  is the material density, and  $t$  is the material thickness. A payload of mass  $m_{\text{payload}}$  located a distance  $d_{\text{payload}}$  from the base produces an additional moment:

$$M_{\text{payload}} = m_{\text{payload}} g d_{\text{payload}}. \quad (12)$$

Summing moments about the base and comparing to Equation (10) yields

$$\frac{P_o \pi D_{\text{robot}}^3}{8} = m_{\text{robot}} g \frac{L_{\text{robot}}}{2} + m_{\text{payload}} g d_{\text{payload}}. \quad (13)$$

Solving for the critical length shows the dependence on pressure, payload mass, and payload location:

$$L_{\text{robot}} = \sqrt{\frac{\frac{P_o \pi D_{\text{robot}}^3}{8} - m_{\text{payload}} g d_{\text{payload}}}{2\pi D_{\text{robot}} t \rho g}}. \quad (14)$$

When the payload sits at the tip ( $d_{\text{payload}} = L_{\text{robot}}$ ) this gives the longest guaranteed span for this payload weight,

$$L_{\text{robot}} = \frac{-m_{\text{payload}} + \sqrt{m_{\text{payload}}^2 + \frac{\pi^2 D_{\text{robot}}^4 t \rho P_o}{2g}}}{2\pi D_{\text{robot}} t \rho} \quad (15)$$

though longer lengths can be crossed when the payload is closer to the base.

## IV. EXPERIMENTAL

In this section, we perform a series of experiments to validate the above models and to show the range of object deployment tasks that a soft everting robot can carry out.

### A. Object Transportation

1) *Object transport on flat surfaces:* Initial testing with moving payloads on flat surfaces saw no measurable effects on growth as expected, and growth proceeded smoothly when the servos were used to limit the friction. To better understand the effects of the material storage and need for the servos, a series of flat-ground trials were carried out. The soft everting robot was grown on flat ground while carrying a 1500 g spherical payload. The robot pressure,  $P_o$ , was varied between 0.51 kPa

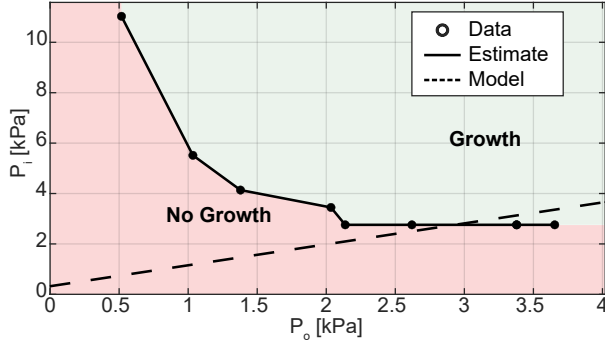


Figure 3. Chart showing combination of  $P_o$  and  $P_i$  which produce growth without servo assistance. Each data point represents a pair of  $P_o$  and  $P_i$ . The dashed curve shows the theoretical minimum  $P_i$  for growth predicted by Eq. (7) which assumes no air flow out of the robot tip. Data indicates significant air flow at low  $P_o$  values, requiring large commanded  $P_i$ .

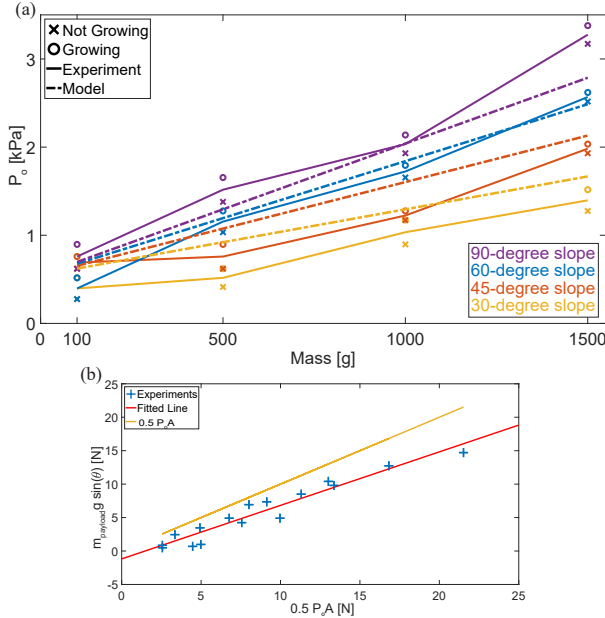


Figure 4. (a) Maximum payload mass transported up an incline as a function of  $P_o$ . Individual curves represent slopes of 30°, 45°, 60°, and 90° and model is plotted for comparison. (b) Corresponding values of  $0.5 P_o A_c$  plotted against  $m_{\text{payload}} g \sin \theta$  for all collected data. Best fit intercept predicts a  $F_{\text{loss}}$  value of 3.6 N.

and 3.65 kPa, and, for each pressure, the inner pressure  $P_i$  was increased in 0.69 kPa increments until growth began. Figure 3 shows the resulting working combinations of  $P_o$  and  $P_i$ , along with the model made by combining Equations (1) and (3). While  $P_i$  is near the model prediction for high values of  $P_o$ , at low  $P_o$ , the commanded inner pressure is significantly higher. This is due to the fact that when  $P_i$  is large enough, it will break the seal at the tip of the robot and air will flow instead of reaching the command pressure [23]. As such, without servos, the range of feasible growth combinations is small and will be even smaller when the payload weight is added.

2) *Object transport on inclined surfaces:* We next verify the effects of payload weight on vertical growth, as modeled in the equations in Table I. A soft evertng robot was grown up an angled slope while lifting a 9.5 cm diameter spherical payload. The payload mass was varied from 100 g to 1500 g while the slope angle was varied from 30° to 90°. A fixed  $P_i$

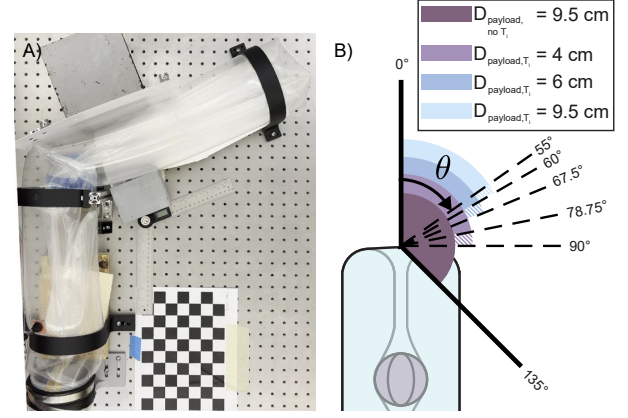


Figure 5. (a) The test rig showing a (blue) payload that failed to traverse a fixed angle bend when tail tension was present. (b) Experimental results for bend angles from 45° to 135°. With tail tension, larger payload diameter could only pass acute angle turns (< 90°). With tail tension removed every payload traversed all tested angles without jamming.

value of 1.4 kPa was used to reduce the force needed from the servos. With the payload on the slope,  $P_o$  was raised until growth began then lowered until motion stopped, producing lower,  $\times$ , and upper bounds,  $\circ$ , on the growth threshold.

Figure 4(a) shows these thresholds along with the model lines. As expected, larger mass and steeper slope require higher  $P_o$ .

To determine the best fit for  $F_{\text{loss}}$ , Figure 4(b) plots  $0.5 P_o A_c$  against  $m_{\text{payload}} g \sin \theta$  for all data, yielding a linear fit with vertical offset of 3.6 N. This offset matches the  $F_{\text{loss}}$  predicted using tests with equivalent material thickness, 4.1 N [30]. The only place where the model significantly under-predicted the necessary  $P_o$  value was in pure vertical growth. Payloads heavier than 500 g tended to stall at the corner, so for the 90° slope the payload was placed above the fold. Still, this large turn angle caused significant friction as the material was pulled around it, explaining the larger pressure.

3) *Object transport through turns:* A soft evertng robot steers by buckling material on the inner surface while the outer surface remained in tension, curving the body toward the buckled side. This introduces wrinkles that distort the shape and size of the internal cross-section, which could hinder payload movement. While most steering is *Continuous*, produced by small distributed actuation along the entire length, *Discrete* steering concentrates the bend at a single location and produces larger internal wrinkles. We focus on payload deployment around discrete bends as a worse case scenario.

Payloads of variable length and diameter were grown around increasing bend angles  $\theta$ , up to 135°, until they could no longer successfully move (Figure 5(A)). The tests were performed both with and without tail tension  $T_t$ . Walls on the inner and outer sides constrained the robot to a prescribed bend angle, and the tip was taped to a rigid bracket to prevent backward motion, mimicking a bend occurring mid-deployment. The final successful angle and first failed angle were noted for each test. During testing, no effect of length was seen, so results (Figure 5(B)) show successful angle range as a function of payload diameter. With  $T_t$ , larger diameters consistently jammed at smaller angles. Eliminating tail tension markedly



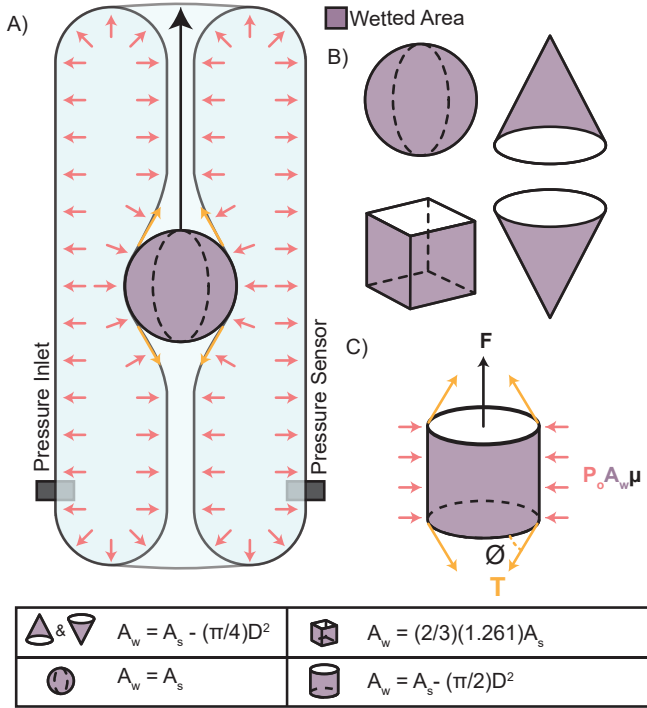


Figure 6. (a) Experimental setup for the pull-out force measurement. (b) Geometries used in the shape-series test, with wetted areas highlighted in purple. (c) Free-body diagram of forces acting on cylinders in the surface-area series test. (d) Table of wetted area calculations by shape.

improved performance and all tested lengths and diameters passed through the maximum tested bend,  $\theta = 135^\circ$ . When the tension is high, the tail is forced tightly against the inner wall of the bend, constricting the passage and causing interaction between payload and the wrinkled surface. This further highlights the benefit of servos in payload deployment.

### B. Object Grasping

1) *Pull-out Force*: To initially validate the grasping model in Table I, a short length of soft everting robot structure was secured such that it could not grow (Fig. 6). This arrangement isolates the gripping conditions that depend on  $P_o$  and the membrane's mechanical properties. Using this simplified geometry, we can estimate normal forces and friction coefficients without the added variables from growth dynamics.

For each test, the gripper was pressurized to 5 kPa and conformed around a payload suspended on a fishing line. The other end of the fishing line was pulled upward by a motorized force test stand with force transducer (M7-100, Mark-10), forcing the payload to slip. During each pull-out trial, the force stand advanced at  $50 \text{ mm min}^{-1}$  and stopped at full extension or a maximum force of 50 N.  $P_o$  was first set to 5 kPa and then allowed to slowly decrease from small inherent leaks. Each run provided a continuous record of the pull-out force ( $F$ ) versus the everting gripper pressure from the pressure sensor ( $P_o$ ). Two experimental series were executed:

**Surface Area series.** Cylinders of 4.0 cm in diameter and lengths from 6.0 cm to 20.0 cm were printed from Polyethylene Terephthalate Glycol (PETG). Some were wrapped in

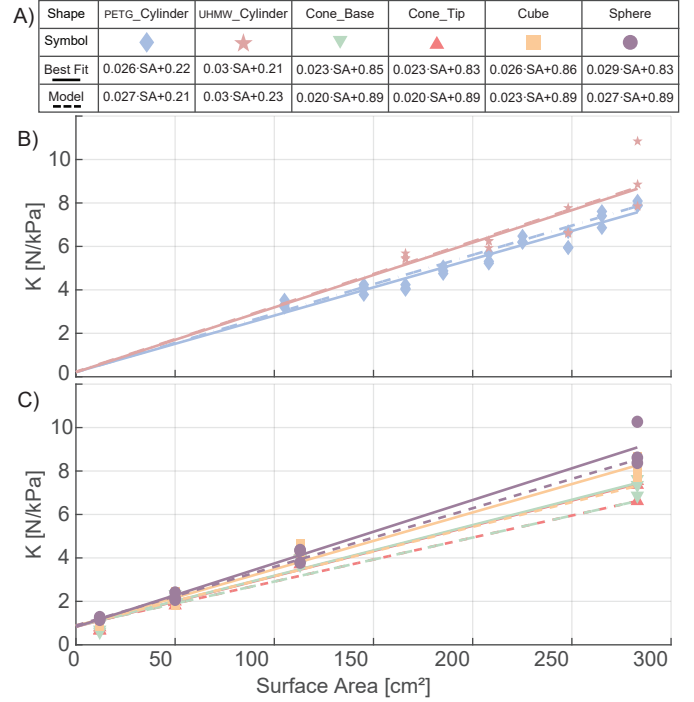


Figure 7. (a) Legend summarizing all pull-out test groups, showing their symbols, experimental best-fit lines, and the theoretical curve from Equation (7). (b) Effective contact area ( $K = \Delta F / \Delta P$ ) during pull-out versus surface area for cylinders with different friction coefficients. (c) Effective contact area during pull-out versus surface area for the various object geometries tested.

UHMW tape to create two friction levels. Static friction versus LDPE was measured at  $\mu_{\text{PETG}} = 0.27$  and  $\mu_{\text{UHMW}} = 0.30$ .

**Shape series.** Four geometries were tested: a sphere, a cube, and a cone tested base first and tip first. Four sizes of each shape were used with equal total surface area, based on sphere diameters of 2.0 cm, 4.0 cm, 6.0 cm and 9.5 cm.

The pull-out force data was approximately linear with pressure, so after collection a least squares line was fit and the slope,  $K$ , was extracted. The resulting  $K$  values are plotted in Fig. 7(B) and (C). The surface area series (Fig. 7(B)) show that both PETG and UHMW data display linear trends with slightly different slopes (Figure 7(A)). This matches Equation 7, as the relationship between  $A_w$  and  $K$  is governed by  $\mu$ , so a larger  $\mu$  yields a steeper line. The intercept is set by the wrap component, which should not vary with a set end geometry. Without the wrap component, the surface area alone underestimates  $K$  especially for short cylinders, where membrane wrap becomes significant. Adding the wrap term brings the prediction within a mean absolute percentage error of 6% of the PETG data and 8% of the UHMW data.

Fig. 7(C) similarly summarizes the shape series. When the shape changes, the wetted area changes, altering the slope as the membrane grips the surface to a different extent. The wetted areas used in the model are shown in Figure 6. Rotationally uniform shapes have the side projected surface as  $A_w$ , but the sharp edges of the cube increase effective contact by a factor of 1.261, equivalent to the ratio of the square's hydraulic-equivalent diameter to the nominal diameter.

2) *Payload Slippage*: With the model verified without inner pressure, we now experimentally determine the conditions

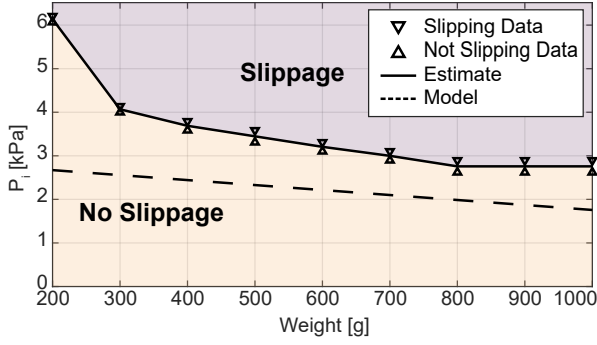


Figure 8. Plot showing  $m_{\text{payload}}$  versus  $P_i$  for a  $60^\circ$  slope at a constant  $P_o = 2.90$  kPa. The orange region marks pressure levels where the payload remains stationary, and the purple region marks pressure levels where it slips.

when payload slip begins inside the soft everting robot. The servos were held in place, so that growth was still restricted. Any observable motion, therefore, indicated payload slip rather than growth. The robot, with a constant  $P_o$  (2.90 kPa), was placed on a  $60^\circ$  incline while a spherical payload with mass ranged from 200 g to 1000 g rested midway along its length. The commanded  $P_i$  was increased stepwise, pausing after each increment to re-equilibrate and check for slip. When airflow through the inner membrane caused slippage,  $P_i$  was briefly lowered to stabilize the payload within the robot before continuing. The slip threshold for each mass was defined as the lowest  $P_i$  that produced noticeable translation.

Fig. 8 plots  $m_{\text{payload}}$  against the slip threshold  $P_i$ . Triangles mark the upper and lower bounds of slippage, while the solid line marks the midpoint for an empirical slip boundary. The critical  $P_i$  decreases monotonically with payload mass because heavier objects require less differential pressure to overcome static friction, which the model line matches well, though it under-predicts the necessary  $P_i$ , again likely due to the air flow rate of the inner pressure. The viable control window for  $P_i$  narrows with increasing payload, but since all payloads in Figure 4 could be deployed with a  $P_i$  of 1.4 kPa, there remains a significant range of control across the full mass range tested. Incorporating a one-dimensional flow analysis for  $P_i$  into Equation (7) would yield a more accurate operating envelope for payload delivery.

3) *Multi-Object Deployment*: The effect of distribution across multiple payloads on slip and carrying were also investigated. We tested three arrangements whose weights each sum to 1500 g with either one, two, or three spherical payloads. In the split cases, the spheres were evaluated while touching in series and while separated by sealed body sections. All trials shared the same inflation used in testing the slip on a slope section. Both growth start and stop and slip start and stop were observed. This data in Figure 9 shows that dividing mass has little effect on growth but significantly affects slip. Multiple payloads separated by enough distance to see full wrap effects (Figure 9(B)) showed the highest  $P_i$  value before slip.

### C. Challenging Terrain

1) *Hole Restriction*: Able to compress through apertures smaller than their body's diameter, soft everting robots are well suited to navigating confined spaces. To analyze payload

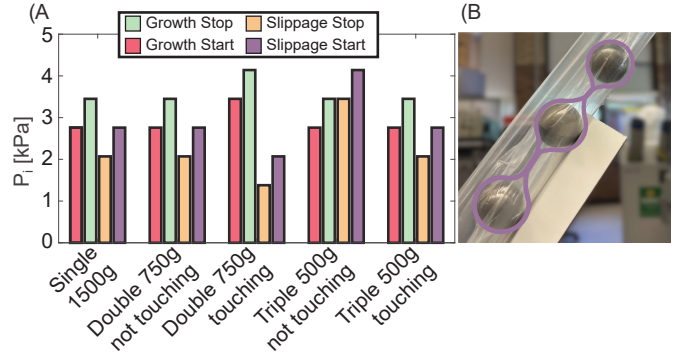


Figure 9. (a) Plots showing the  $P_i$  values at which growth starts and stops and at which slippage starts and stops for each test case. (b) A three object payload, each a sphere of 500 g, positioned on the slope without touching one another. Line shows how the robot material separates the objects so they do not interfere, leading to higher slip resistance compared to touching objects.

delivery in such environments, it is important to evaluate the robot's ability to move objects through holes with minimal clearances. We conducted an experiment to quantify the robot's ability to move payloads through nearly size-matched circular apertures. Four objects with nominal diameters of 6.0 cm were tested against four hole diameters, 6.8 cm, 6.4 cm, 6.2 cm and 6.01 cm, using the apparatus shown in Fig. 10(A). The last diameter is an estimate for the smallest hole that a 6.0 cm payload could pass when accounting for the robot material:

$$D_{\text{hole}} = D_{\text{payload}} + \frac{4tD_{\text{robot}}}{D_{\text{payload}}}. \quad (16)$$

These apertures provide clearances from approximately 0.01 cm up to 0.8 cm. Before each trial the robot body was pre-inserted through the hole so that any failure could be attributed solely to limitations in object transport.

For every object–aperture pairing, ten trials were performed with randomized initial orientations. Preliminary observations confirmed that object orientation critically affects success when clearance is minimal, as slight misalignments can induce jamming. However, despite random start orientations, for some objects the combined action of the ground plane and the tail's positive pressure seal aligned the objects far more reliably than we had expected, consistently orienting them into a favorable attitude before they entered the hole. The success rates across ten trials are summarized in Fig. 10(A)ii. All objects, except the cylinder, achieved a 100 % success rate for a 6.4 cm aperture. The cylinder failed because its most stable alignment was on its side (Figure 10(A)iii) where it could not pass through the hole. Increasing the cylinder's height mitigated this effect by encouraging axial alignment, highlighting the potential of tailoring object geometry to promote self-alignment. Both the cone and the sphere reached 100 % success at the 6.2 cm aperture, although these trials produced noticeable wear on the robot membrane. At the smallest clearance (6.01 cm), some success was achieved but at the cost of significant membrane wear at the hole edge.

2) *Gap Crossing*: Our final experiment characterized the robot's capacity to bridge an unsupported horizontal gap while carrying a payload, first in a cantilevered configuration growing outward from one platform and then in a two end

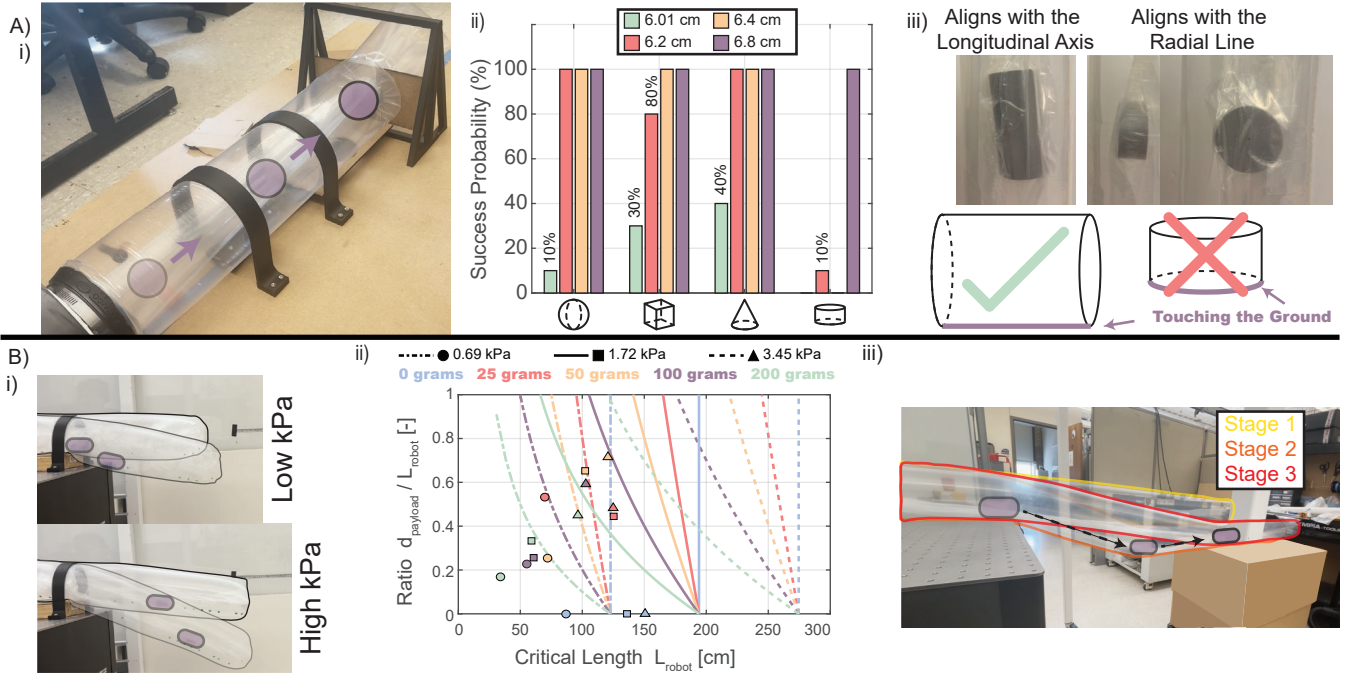


Figure 10. (a) Hole restriction experiments: (i) experimental setup showing the robot deploying a payload through a circular aperture, (ii) success rate over 10 trials for each nominal 6.0 cm shape (the cube is inscribed) passing through apertures of different diameters, (iii) images illustrating how payload geometry influences realignment inside the robot. (b) Gap crossing experiments: (i) images showing the influence of  $T_t$ , and consequently  $P_o$ , on gap-crossing performance, (ii) cantilever results with raw data and the model of Equation 14, (iii) demonstration that growing across the gap first, then transporting the payload, allows the robot to span larger gaps with heavier payloads.

supported configuration where the robot spans the gap before the payload is transported. The procedure tests the model shown in Table I. In each trial, the robot started on a fixed platform and then grew outward until either the payload reached the end or the robot buckled (Figure 10(B)i). The trials varied the payload mass from 0 g to 200 g and varied the internal inflation pressure  $P_o$  by artificially increasing the tail tension to determine the maximum length that could be reached before collapse. The growth, including the vertical tip deflection and the deployed length, were recorded by video.

The data, shown in Fig. 10(B)ii, reveals clear effects of payload and pressure on failure length. For a given pressure, there exists a critical length beyond which the structure cannot support even its own weight. This limit then decreases when a payload is introduced or increases when the pressure is raised. These observations provide an empirical map of sagging and collapse that supplements the moment-balance relations in Equations (10)–(13). However the models over predict the collapse lengths, potentially due to the conditions where the robot left the table surface leading to easier buckling at that point. A follow-up set of tests investigated whether the robot could move payloads over larger gaps by first crossing without the payload and then transporting the object across. The robot grew across a gap to a surface located 15 cm below the starting platform. After contact with the opposite edge, a 500 g mass was carried inside the tail, and the robot attempted to grow further. This payload is substantially heavier than the 200 g limit used in the cantilevered trials. Nevertheless, in Figure 10 (B)iii, the robot can be seen successfully carrying the 500 g mass across a 115 cm gap. This improved performance can be attributed to the difference in loading conditions. During

the three-point bending scenario the lower surface of the membrane remained in tension, which allows the thin wall to support a larger load compared to the cantilevered configuration which placed the lower surface in compression. These results indicate that controlling object placement within the robot, possible through intentional slipping within the tail, can extend the terrains which can be crossed.

## V. DISCUSSION

The experimental results detailed in Section IV corroborate the analytical models of Section III and delineate the soft everted robot's operating envelope. In the object-transport trials, the onset of growth obeyed the pressure inequalities of Equation (6): on level ground and without servos, growth commenced only when  $P_i$  and  $P_o$  exceeded static friction. Inclined-surface tests with servos further confirmed the linear dependence of the required  $P_o$  on  $m_{\text{payload}}g \sin \theta$ , validating the gravity term in Equation (6). A small vertical intercept in the pressure–force fit represents an orientation-independent loss  $F_{\text{loss}}$  which matches previous experimental results. Vertical climbs exposed bend-induced jamming, which was validated by the results of testing deployment around bends, suggesting that future models include segment-specific friction coefficients. Nevertheless, the robot lifted a 1.5 kg payload vertically, demonstrating the efficacy of combining internal pressure with tail drive.

Grasping experiments (Section IV-B) upheld the extended eversion gripper model. The measured linear force–pressure curves matched Equation (7) once the membrane-wrap term  $\frac{1}{2}A_c \cos \phi$  was included. Shape-series tests showed that, with an appropriate wetted-area estimate, the same model predicts

holding forces for a range of shapes spheres, cubes, and cones. Hence gripping performance for novel geometries can be predicted quantitatively.

Finally, terrain studies show that many beneficial features of movement by growth are preserved when deploying payloads in this manner, and the results suggest some mitigation strategies for observed effects. Hole-restriction trials revealed that near-zero clearance yields intermittent jams, but utilizing Equation (16) elevates success to nearly 100%. Ground contact and tail tension can align objects if shaped well, indicating that deliberate orientation control could further reduce jamming. Gap-crossing tests demonstrated a critical span length. Higher pressure extended reach but with diminishing benefit, bounded by material strength. The results furnish a pragmatic design rule: for a specified gap and payload, trajectory adjustment or supplemental supports can better guarantee success.

Overall, the results indicate that payload deployment using soft everting robots is a promising method to deploy a range of sensor, actuator, and other payloads. There are some limitations that were found in this work. The material friction caused significant wear on the robot, requiring frequent changing of robot body tubes. This could be mitigated by higher quality materials. Additionally, causing a payload to emerge at a desired point required precise timing. While we proved repositioning of passive payloads is theoretically possible, achieving it in practice will require new planning strategies or the creation of active payloads.

## VI. CONCLUSION

This work delivers an integrated framework that links theory with practice for payload deployment using a soft everting robot. Analytical models establish conditions for successful growth while carrying a load, predict the gripping force that restrains an object within the tail, and outline the pressure and span limits that govern passive gap crossing. A comprehensive set of trials confirms those predictions and shows that the robot can transport objects up to 1500 g through slopes, tight apertures, and unsupported gaps with only minor path adjustments. The agreement between the model and the data demonstrates that the key mechanical factors are now understood well enough to guide mission planning and payload packaging. Future studies will extend the approach to dynamic maneuvers, incorporate variable-stiffness skins to suppress sag, and investigate closed-loop strategies that couple onboard sensing with autonomous routing, broadening the range of tasks accessible to soft everting robots in real environments.

## REFERENCES

- [1] Daniela Rus and Michael T Tolley. Design, fabrication and control of soft robots. *Nature*, 521(7553):467–475, 2015.
- [2] Cecilia Laschi, Barbara Mazzolai, and Matteo Cianchetti. Soft robotics: Technologies and systems pushing the boundaries of robot abilities. *Science Robotics*, 1(1):eaah3690, 2016.
- [3] Cosimo Della Santina, Manuel G. Catalano, and Antonio Bicchi. *Soft Robots*, pages 1–15. Springer Berlin Heidelberg, Berlin, Heidelberg, 2020.
- [4] Margaret M. Coad, Laura H. Blumenschein, Sadie Cutler, Javier A. Reyna Zepeda, Nicholas D. Naclerio, Haitham El-Hussieny, Usman Mehmood, Jee-Hwan Ryu, Elliot W. Hawkes, and Allison M. Okamura. Vine Robots. *IEEE Robotics & Automation Magazine*, 27(3):120–132, 2020.
- [5] Laura H Blumenschein, Margaret M Coad, David A Haggerty, Allison M Okamura, and Elliot W Hawkes. Design, modeling, control, and application of everting vine robots. *Frontiers in Robotics and AI*, 7:548266, 2020.
- [6] Elliot W. Hawkes, Laura H. Blumenschein, Joseph D. Greer, and Allison M. Okamura. A soft robot that navigates its environment through growth. *Science Robotics*, 2(8):eaan3028, 2017.
- [7] Pascal Auf der Maur, Betim Djambazi, Yves Habert, Patricia Hörmann, Alexander Kübler, Michael Lustenberger, Samuel Sigrist, Oda Vigen, Julian Förster, Florian Achermann, Elias Hampp, Robert K. Katzschnmann, and Roland Siegwart. RoBoa: Construction and Evaluation of a Steerable Vine Robot for Search and Rescue Applications. In *IEEE International Conference on Soft Robotics*, pages 15–20, 2021.
- [8] Ayush Giri, Cédric Girerd, Jacobo Cervera-Torralba, Michael T Tolley, and Tania K Morimoto. Inchgrab: An inchworm-inspired guided retraction and bending device for vine robots during colonoscopy. *IEEE/ASME Transactions on Mechatronics*, 2025.
- [9] Jamie Luong, Paul Glick, Aaron Ong, Maya S. deVries, Stuart Sandin, Elliot W. Hawkes, and Michael T. Tolley. Eversion and Retraction of a Soft Robot Towards the Exploration of Coral Reefs. In *IEEE International Conference on Soft Robotics*, pages 801–807, 2019.
- [10] Nicholas D. Naclerio, Andras Karsai, Mason Murray-Cooper, Yasemin Ozkan-Aydin, Enes Aydin, Daniel I. Goldman, and Elliot W. Hawkes. Controlling subterranean forces enables a fast, steerable, burrowing soft robot. *Science Robotics*, 6(55):eabe2922, 2021.
- [11] Laura H. Blumenschein, Margaret M. Coad, David A. Haggerty, Allison M. Okamura, and Elliot W. Hawkes. Design, Modeling, Control, and Application of Everting Vine Robots. *Frontiers in Robotics and AI*, 7, 2020.
- [12] O. G. Osele, K. Barhydt, N. Cerone, A. M. Okamura, and H. H. Asada. Tip-Clutching Winch for High Tensile Force Application with Soft Growing Robots. In *IEEE International Conference on Robotics and Automation*, 2024.
- [13] Cem Suulker, Sophie Skach, Danyaal Kaleel, Taqi Abrar, Zain Murtaza, Dilara Suulker, and Kaspar Althoefer. Soft Cap for Vine Robots. In *IEEE/RSJ International Conference on Intelligent Robots and Systems*, pages 6462–6468, 2023.
- [14] Nam Gyun Kim and Jee-Hwan Ryu. A Soft Growing Robot Using Hyperelastic Material. *Advanced Intelligent Systems*, 5(2):2200264, 2023.
- [15] Sang-Goo Jeong, Margaret M. Coad, Laura H. Blumenschein, Ming Luo, Usman Mehmood, Ji Hun Kim, Allison M. Okamura, and Jee-Hwan Ryu. A Tip Mount for Transporting Sensors and Tools using Soft Growing Robots. In *IEEE/RSJ International Conference on Intelligent Robots and Systems*, pages 8781–8788, 2020.
- [16] William E. Heap, Nicholas D. Naclerio, Margaret M. Coad, Sang-Goo Jeong, and Elliot W. Hawkes. Soft Retraction Device and Internal Camera Mount for Everting Vine Robots. In *IEEE/RSJ International Conference on Intelligent Robots and Systems*, pages 4982–4988, 2021.
- [17] Gayoung Park, Katalin Schäffer, and Margaret M Coad. Soft everting prosthetic hand and comparison with existing body-powered terminal devices. *arXiv preprint arXiv:2503.01585*, 2025.
- [18] Dongbao Sui, Yanhe Zhu, Sikai Zhao, Tianshuo Wang, Sunil K Agrawal, He Zhang, and Jie Zhao. A bioinspired soft swallowing gripper for universal adaptable grasping. *Soft Robotics*, 9(1):36–56, 2022.
- [19] Haili Li, Jiantao Yao, Chunye Liu, Pan Zhou, Yundou Xu, and Yongsheng Zhao. A bioinspired soft swallowing robot based on compliant guiding structure. *Soft Robotics*, 7(4):491–499, 2020.
- [20] Mingge Li, Xiaoming Huang, Quan Liu, and Zhongjun Yin. A variable stiffness bioinspired swallowing gripper based on particle jamming. *Soft Robotics*, 12(1):56–67, 2025.
- [21] Samuel E Root, Daniel J Preston, Gideon O Feifke, Hunter Wallace, Renz Marion Alcoran, Markus P Nemitz, Jovanna A Tracz, and George M Whitesides. Bio-inspired design of soft mechanisms using a toroidal hydrostat. *Cell Reports Physical Science*, 2(9), 2021.
- [22] Joseph D. Greer, Tania K. Morimoto, Allison M. Okamura, and Elliot W. Hawkes. A soft, steerable continuum robot that grows via tip extension. *Soft Robotics*, 6(1):95–108, 2019.
- [23] Ji-hun Kim, Jaehyung Jang, Sang-min Lee, Sang-Goo Jeong, Yong-Jae Kim, and Jee-Hwan Ryu. Origami-inspired New Material Feeding Mechanism for Soft Growing Robots to Keep the Camera Stay at the Tip by Securing its Path. *IEEE Robotics and Automation Letters*, 6(3):4592–4599, 2021.
- [24] Dongoh Seo, Nam Gyun Kim, and Jee-Hwan Ryu. Inflatable-structure-based working-channel securing mechanism for soft growing robots. *IEEE Robotics and Automation Letters*, 9(9):7755–7762, 2024.
- [25] Sidney Nimako Boateng, Shashwat Singh, Mustafa Ugur, Sicheng Wang, Max Kramer, Isaac Osei, Olivia Sobek, Melisa Orta Martinez, F. Zeynep



- Temel, and Laura H. Blumenschein. Heterogenous collaboration: A new approach for search and rescue operations. In *IEEE International Symposium on Safety Security Rescue Robotics*, pages 142–147, 2024.
- [26] Margaret M. Coad, Rachel P. Thomasson, Laura H. Blumenschein, Nathan S. Usevitch, Elliot W. Hawkes, and Allison M. Okamura. Retraction of Soft Growing Robots Without Buckling. *IEEE Robotics and Automation Letters*, 5(2):2115–2122, 2020.
- [27] RL Comer and Samuel Levy. Deflections of an inflated circular-cylindrical cantilever beam. *AIAA journal*, 1(7):1652–1655, 1963.
- [28] Robert W Leonard. *Structural considerations of inflatable reentry vehicles*. National Aeronautics and Space Administration, 1960.
- [29] Ciera McFarland and Margaret M Coad. Collapse of straight soft growing inflated beam robots under their own weight. In *IEEE International Conference on Soft Robotics*, pages 1–8, 2023.
- [30] Laura H Blumenschein. *Design and Modeling of Soft Growing Robots*. Stanford University, 2019.